The International Journal of Advanced Manufacturing Technology
https://doi.org/10.1007/s00170-025-17331-8

ORIGINAL ARTICLE

Investigation of SiC decomposition in laser powder bed fusion: impact of scanning strategies

Mohamed Abdelmoula[1,2,3] · Alejandro Montón Zarazaga[4] · Gökhan Küçüktürk[1] · Francis Maury[5] · David Grossin[5] · Marc Ferrato[6] · Duran Kaya[7]

Received: 25 July 2025 / Accepted: 23 December 2025
© The Author(s) 2026

Abstract
SiC is susceptible to decomposition into Silicon and Carbon during. D-LPBF when exposed to temperatures above its decomposition threshold. This study investigates the impact of various laser scanning strategies; linear, concentric in-out, zigzag, and hexagonal patterns. The temperature history effects of these scanning strategies were investigated to observe the SiC degradation and its impact on the phase composition. A thermal simulation model was developed to analyse temperature evolution under each scanning pattern. Results showed that concentric in-out, zigzag, and hexagonal strategies involving frequent changes in laser direction generated localised high-temperature peaks. These peaks enhanced layer bonding but also triggered partial decomposition of SiC. However, the linear strategy lacked sufficient thermal peaks, resulting in poor interlayer adhesion and overlapping defects. Quantitative phase analysis was conducted using Rietveld refinement of X-ray diffraction (XRD) data. The hexagonal strategy resulted in the highest decomposition, yielding 18% Si and 5.66% C, while the zigzag strategy demonstrated the lowest decomposition, with 8.84% Si and 1.07% C. The study highlights the critical role of scanning strategy in balancing layer quality and decomposition, underscoring the need for optimised scanning patterns to mitigate degradation in LPBF of ceramics, such as SiC.

Keywords LPBF · SiC · Simulation · Phase analysis · Rietveld refinement

1 Introduction

Silicon Carbide (SiC) is a crucial ceramic material widely used in cutting-edge applications, including sensors, biomedical devices, aerospace, power electronics, and composite materials [1–5]. Its significance lies in its exceptional characteristics, including high compressive strength, high elastic modulus, low density, chemical and thermal stability, outstanding hardness, wear resistance, and advanced optical quality [6–8]. Traditionally, SiC components have

✉ Gökhan Küçüktürk
gkucukturk@gazi.edu.tr

Mohamed Abdelmoula
mohamedeid@aun.edu.eg

Alejandro Montón Zarazaga
alejandromonton@unizar.es

Francis Maury
francis.maury@ensiacet.fr

David Grossin
david.grossin@ensiacet.fr

Marc Ferrato
marc.ferrato@mersen.com

Duran Kaya
durankaya@gazi.edu.tr

1 Department of Mechanical Engineering, Faculty of Engineering, Gazi University, Ankara 06570, Turkey

2 Department of Mechanical Design and Production, Faculty of Engineering, Assiut University, Assiut 71515, Egypt

3 Mechanical Engineering Department, Faculty of Engineering, Sphinx University, New Assiut 17090, Egypt

4 Centro Universitario de la Defensa, Zaragoza, Spain

5 Univ. Toulouse, Toulouse INP, CNRS, CIRIMAT, 4 allée Emile Mons, BP44362, Toulouse Cedex 4 31030, France

6 Mersen Boostec, Zone Industrielle Bazet ouest, Bazet 65460, France

7 Project Coordination Implementation and Research Center, Gazi University, Ankara 06560, Turkey

Published online: 11 April 2026

been manufactured using well-established industrial approaches, such as pressing, casting, and extrusion [9–11], which have been used since the 1990 s [9]. However, some specialised applications demand more sophisticated manufacturing approaches beyond the capabilities of these traditional methods. Additive Manufacturing (AM) offers a promising solution for fabricating complex designs. AM is an innovative technology that constructs parts directly from 3D CAD models through a layer-by-layer process [10]. The American Society for Testing and Materials (ASTM) classifies seven main AM techniques: binder jetting, vat polymerisation, material jetting, direct energy deposition, sheet lamination, and Laser Powder Bed Fusion (LPBF).

Among the various AM techniques applicable to SiC, such as photopolymerization, material jetting, extrusion, and binder jetting, LPBF has recently gained significant attention for its capability to fabricate complex components [11–14]. LPBF of SiC is divided into two main approaches: Direct LPBF (D-LPBF), which uses pure SiC powder as feedstock, and Indirect LPBF (In-LPBF), where SiC powder is mixed with a binder material.

Previous research has focused on the In-LPBF of SiC and its process parameters. Meyers et al. [15] studied In-LPBF of reaction-bonded SiC using silicon as a binder material. They investigated the effects of varying laser power and scanning speed while keeping other parameters constant. Their work produced complex SiC geometries with high relative density, which was further improved through densification processes. Liu et al. [16] increased the relative density of SiC ceramic parts produced by In-LPBF using cold isostatic pressing (CIP) and reaction sintering (RS). Song et al. [20] focused on optimising the structure of SiC/Si composites using In-LPBF. Streek et al. [17] examined the sintering of Si/SiC powder composites (with Si as a binder) under various laser powers, successfully built SiC parts, but with residual Si. Löschau et al. [18] also studied the In-LPBF of SiC powder, employing dissimilar laser powers and scanning speeds to print various complex shapes. Geng et al. [19] demonstrated that the incorporation of Al_2O_3–Y_2O_3 additives in D-LPBF of SiC promotes liquid-phase formation and accelerates densification while suppressing SiC decomposition. Wang et al. [20] reported that silicon addition through hybrid laser PBF and chemical vapour infiltration processing significantly improved microstructural integrity and mechanical strength by enhancing interparticle bonding and reducing residual porosity. Despite these advancements, previous studies reveal that SiC's In-LPBF involves a costly manufacturing process. This typically includes preparing the SiC-binder composite, followed by laser sintering, debinding, sintering, and densification. Additionally, challenges such as shrinkage and achieving satisfactory physical and mechanical properties remain significant obstacles to using In-LPBF with SiC and ceramics in general [13, 21].

D-LPBF can be regarded as one of the most advantageous AM techniques for ceramic materials, as it enables direct printing without the need for feedstock modification. In contrast to many other AM techniques that require the incorporation of binding agents or additives to facilitate processing, D-LPBF utilises pure ceramic powders. For example, material jetting techniques necessitate mixing ceramic powders with photocurable resins, where densification primarily occurs within the polymeric matrix rather than through ceramic–ceramic bonding. By eliminating such dependencies, the D-LPBF process allows the fabrication of ceramic components with high dimensional accuracy and minimal shrinkage. Aforementioned limitations that are typically observed in binder-based AM techniques during debinding or sintering stages. Moreover, D-LPBF often does not require post-processing steps such as debinding and sintering, further enhancing its efficiency and suitability for the direct fabrication of dense, geometrically precise ceramic parts, in contrast to other AM techniques that necessitate post-processing steps [22, 23].

Although D-LPBF could overcome challenges encountered by other AM techniques, there are still barriers preventing D-LPBF from being applied efficiently to the AM of SiC. The high sintering point and rapid sintering rate of SiC during D-LPBF generate significant high-temperature gradients along the scanning path. The varying temperature history leads to the initiation and propagation of cracks, the development of residual stress, and the distortion of the part upon removal from the support structure [24, 25]. Numerous earlier studies focused on finding a solution to these difficulties by applying preheating onto the powder bed to decrease the temperature difference and mitigate the effect of the high melting point of ceramic powder [26, 27]. However, the strategies proposed by these studies were struggled by difficulties, which were not practically feasible.

Moreover, the success of the D-LPBF approach strongly depends on the comprehensive optimisation of laser processing parameters, including laser power, scanning speed, hatch spacing, and scanning strategy. In the author's previous studies, which demonstrated the feasibility of fabricating SiC using LPBF and highlighted that process parameter optimisation is both feasible and highly effective [14, 28, 29]. Furthermore, the authors found that the scanning strategy plays a critical role in determining the quality of the fabricated parts and in mitigating defect formation during the D-LPBF process. Additionally, the authors have investigated several scanning strategies and found that hexagonal and zigzag patterns yielded auspicious results, achieving up to 84% relative density without any post-densification treatments and, in contrast, maintaining the capability to

fabricate geometrically complex components. For further details on the influence of scanning strategies in the D-LPBF of SiC, readers are referred to our previous work [30].

A significant challenge with SiC D-LPBF is that it lacks a liquid phase and decomposes at temperatures above 2800 °C. As a result, many researchers prefer In-LPBF methods over direct approaches [9–15]. The author's previous study [30] highlighted the decomposition process occurring during LPBF, where SiC breaks down into Si and C. This decomposition poses a major challenge, adversely affecting the mechanical and physical properties of SiC parts produced via D-LPBF. Furthermore, our findings indicated that even with optimised D-LPBF processing parameters, it is challenging to keep the temperature far from the decomposition temperature of SiC [30]. This difficulty arises because scanning strategies significantly influence the temperature profile during scanning, creating temperature peaks at specific locations sufficient to induce SiC decomposition.

Therefore, this study aims to examine the temperature history profiles associated with various scanning strategies, including linear, zigzag, concentric in-out, and hexagonal patterns. To achieve this goal, a quantitative phase analysis was performed on both the feedstock powder and the printed SiC parts. The samples were produced by choosing four scanning strategies, assessing SiC decomposition under each strategy. In the experimental part of the study, the numerical model was updated, and this version examines the process parameters used in SiC D-LPBF and collects the temperature history of the sintered area. Rietveld X-ray diffraction (XRD) phase analysis was used to estimate the phase compositions of the produced SiC samples quantitatively.

2 Methodologies

2.1 Numerical modelling

The simulation model employed in this paper has been thoroughly described and developed in our earlier publications [28, 30]. The model includes the laser parameters required for laser-powder bed interaction in the simulation study, temperature dependent material properties, boundary conditions and printer dependent factors. Additionally, the model solves several fundamental governing equations, which are essential for accurately representing the D-LPBF process. The energy equation, Eq. (1), is employed to describe the heat transfer from the laser source to the powder bed, as also reported in [31].

$$\rho\, C_p \frac{\partial T}{\partial t} = \nabla \,.\, (\mathrm{k} \nabla\ \mathrm{T}) + S_h \tag{1}$$

Where ρ , $C_p, T,$ k, t, and S_h is the density, specific heat, temperature, thermal conductivity, time, and the laser heat source, respectively. To describe the laser heat source (Eqs. (5), (3), and (4)) [28], a User-Defined Function (UDF) was developed, compiled, and solved in ANSYS FLUENT 2020R2. Additionally, the SiC material properties as a function of temperature were considered, as per our previous study.

Where ρ, C_p, T, k, t, and $S_h$denote the density, specific heat capacity, temperature, thermal conductivity, time, and laser heat source, respectively. To model the laser heat source (Eqs. (5)–(4)) [31], a User-Defined Function (UDF) was developed, compiled, and implemented in ANSYS FLUENT 2020R2.2

$$S_h = AI_o\alpha\ \exp(-2\,\frac{(x-v_x t)^2+(y-v_y t)^2}{\omega^{\,2}} - \alpha\, z) \tag{2}$$

$$I_o = \frac{2P}{\pi\ \omega^{\,2}} \tag{3}$$

$$\omega\ = \frac{D_b}{2} \tag{4}$$

Where A, I₀, v, t, α, ω, and D_b represent the powder absorptivity, laser intensity, scanning speed, time, absorption coefficient, laser characteristic radius, and laser beam diameter, respectively.

It is worth noting that the laser intensity was calculated based on the laser characteristic radius, as described in Eq. (3) according to [31], while the absorption coefficient was estimated following the approach reported in [32]. Additionally, the temperature-dependent material properties of SiC were incorporated, as detailed in our previous study [33] and presented in Table 1.

The initial and boundary conditions applied in this study are illustrated in Fig. 2. Heat transfer occurs by conduction from the scanned layer to the base plate, as well as by both radiation and convection from the top surface of the layer to the surroundings. Equations (5) and (6) describe these boundary and initial conditions applied to the model. No preheating was applied in this study; hence, the initial temperature was set to T_0 = 300 K in Eq. (5).

$$T\,(x,y,z)_{t=0} = T_O \tag{5}$$

$$-k(\frac{\partial\, T}{\partial\, z}) = \dot{S}_h - h_{cov}\,(T_a - T_s) - \sigma\,\varepsilon(T_a^4 - T_s^4) \tag{6}$$

Where h_{cov}, σ and ε are the convection coefficient, emissivity, and Stefan-Boltzmann constant, respectively.

Table 1 The thermo-physical properties of SiC used in analysis

Property	Value	Ref.
Density, kg/m^3	3210	[30]
Specific heat J/kg·K	$-0.0005\ T^2 + 1.2911\ T + 337.13$, ($T \leq 1273.15$) $0.0201\ T + 1285.9$, ($1273.15 < T < 2200$) 1330, ($T > 2200$) (T, temperature in K)	[14]
Thermal conductivity Wkg·K (T, temperature in K)	$0.0002\ T^2 - 0.4427\ T + 295.88$, ($T \leq 1273.15$) $-8E\text{-}05\ T + 5.676$, ($1273.15 < T < 2200$) 5.5, ($T > 2200$) (T, temperature in K)	[14]
Sintering point, °C	< 2525	[30]
Emissivity	0.7	
Absorptivity	0.55	Measured

Table 2 Dimensions of model geometry

Item	Length (mm)	Width (mm)	Thickness (mm)
Base plate	11	11	0.5
Powder layer	10	10	0.022

Furthermore, the UDF was developed to monitor the sintering process based on the calculated temperature, where any region with a temperate above the sintering point of SiC is considered a sintered region. This helps to test the used process parameters numerically and see if they can sinter the powder layer or not. Regarding the computational domain used to solve the model, Table 2 provides a summary of the model dimensions. The computational model geometry used in the numerical calculations comprises three distinct components: the base plate, the powder layer, and the unscanned powder, as shown in Fig. 1(a), which was created using ANSYS Design Modeller 2020R2. To analyse the thermal history of each scanning strategy, only a single layer was considered, with the behaviour replicated in subsequent layers. The computational domain (mesh) is depicted in Fig. 1(b), where a fine mesh structure is applied to the powder layer and a coarser mesh is used for the base plate and unscanned powder sections.

The numerical solution procedure for the model is illustrated in Fig. 2, starting with the development of the model geometry. A mesh density test was performed to ensure that low-quality mesh sizing did not affect the results. Three meshes were tested, with edge sizes of 5 µm, 2.5 µm, and 2 µm. The test compared the maximum temperature values and the time required to solve one timestep for each mesh size. As shown in Fig. 3, the maximum temperature values stabilised for mesh sizes of 2 µm and 2.5 µm, with a maximum error of 0.13%, which is very low. Consequently, it was determined that any mesh discretisation finer than 2.5 µm effectively reduces errors resulting from poor discretisation while optimising computational time and cost. Therefore, a mesh edge sizing of 2 µm was utilised in this paper. Furthermore, a convergence study was carried out to ensure the numerical stability and accuracy of the model with respect to transient simulation time settings. Several timestep values (1×10^{-5}, 5×10^{-5}, and 1×10^{-4} s) and iteration numbers per timestep (10, 15, and 20) were evaluated. The convergence criteria were established based on the stabilisation of residuals (below 10^{-6} for the energy equation) and the consistency of key simulation outputs, including the maximum sintered region temperature and geometry (length and depth). The results showed that decreasing the timestep below 1×10^{-5} s or increasing the iteration number beyond

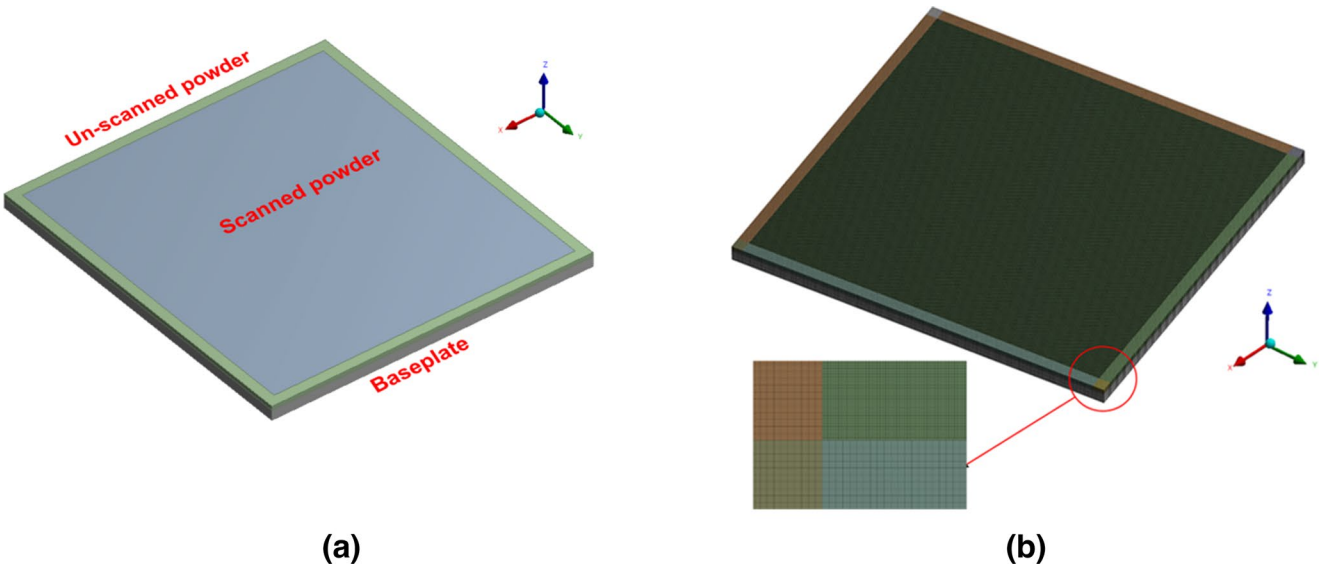


Fig. 1 (**a**) Computational model illustrating the unscanned powder layer, scanned region, and baseplate; (**b**) computational domain used in the analysis. (Not to scale.)

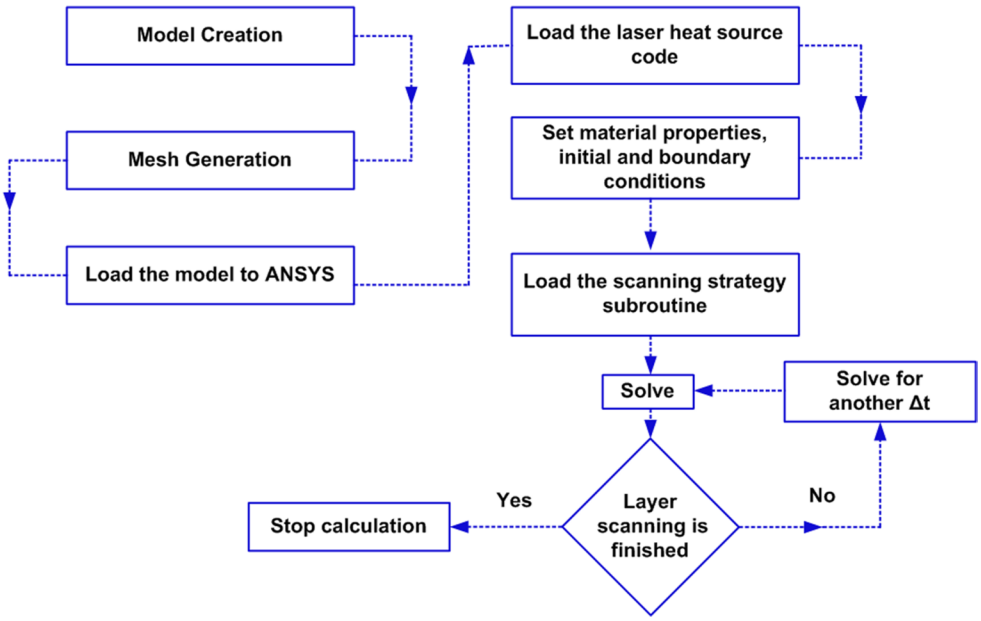


Fig. 2 Flowchart illustrating the procedure for solving the numerical model

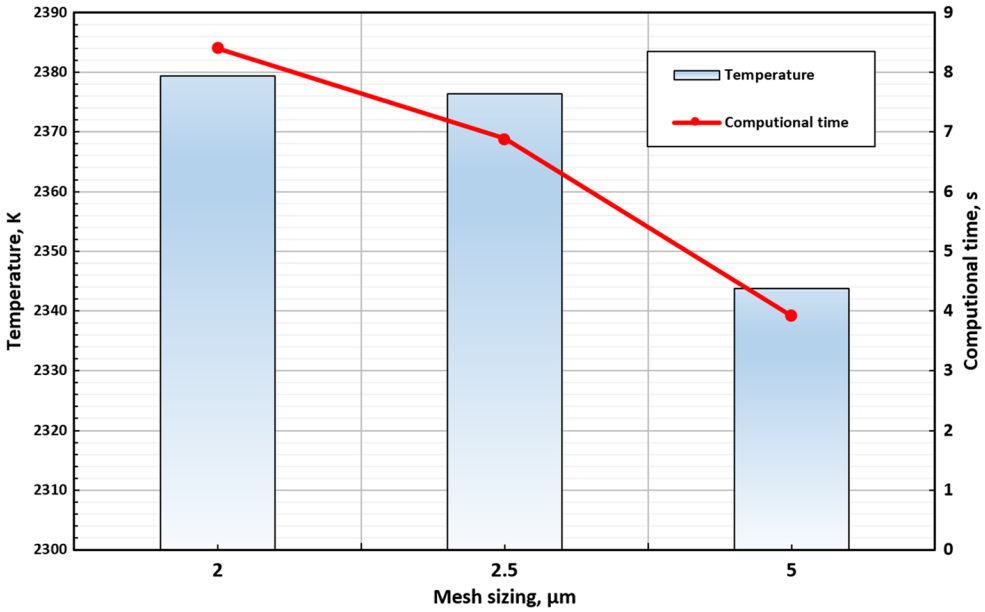


Fig. 3 Mesh density analysis performed with various mesh edge sizes to evaluate their effect on the simulation results and to determine the optimal mesh size for this study

20 led to variations of less than 2% in these key parameters. Therefore, a mesh edge size of 2 μm and a timestep of 1×10^{-5} s with 20 iterations per step were selected as the optimal parameters.

Numerical modelling is a powerful tool for analysing and investigating findings from experimental research in depth. However, to ensure the effectiveness of these numerical models, it is crucial to validate them against experimental data, thereby simulating real-world scenarios and verifying the accuracy of the results obtained from the models. Therefore, in our previous studies, we validated the LPBF model with real-world scenarios of SiC's LPBF and demonstrated that the model could produce results very close to those obtained experimentally. For additional information on the model validation process, the reader is recommended to check our previous studies [28, 30]. The model was formulated using a single-layer domain to isolate the scanning-strategy-dependent temperature response while maintaining computational efficiency. This configuration captures the dominant in-scan thermal gradients that govern the decomposition of SiC. Although multi-layer heat accumulation is not explicitly included, its influence is conceptually discussed based on the expected increase in baseline temperature with layer buildup.

2.2 Experimental analysis

2.2.1 Feedstock and D-LPBF

The α-SiC powder used in this study was supplied by Mersen Boostec® (France) with a purity of 98.5% and a median particle size (d_{10}) of 20 µm (The d_{10}value is approximately **4 µm**, while the d_{90}value is around **30 µm**). The particle distribution diagram is shown in Fig. 4(a). The powder morphology, examined by SEM images in Fig. 4(b), exhibited irregular particle shapes, which can increase inter-particle friction and potentially lead to difficulties during layer deposition. Such irregularity may also increase friction between particles and the baseplate, thereby affecting the uniformity of powder spreading. Consequently, it was necessary to assess the powder's flowability prior to its use in the LPBF process. Powder flowability was evaluated using the dynamic angle of repose method, a standardised characterisation technique recommended by ASTM for assessing the flow behaviour of powders in additive manufacturing applications [33]. In this study, the angle of repose was measured using a Powder Characteristics Tester (PT-S, Hosokawa Micron Ltd, U.K.), yielding an average value of 41° [28], which falls within the acceptable range for powder bed-based AM processes [33, 34]. To ensure strong adhesion of the first printed layers to the build platform, SiC round plates (Mersen Boostec®, France) with a diameter of 65 mm were used as the baseplates. These plates were securely attached to the machine's build platform using a Permabond adhesive, as shown in Fig. 4(c). Initial deposition trials confirmed that the SiC powder could be spread uniformly and smoothly across SiC round plates, as illustrated in Fig. 4(d). Furthermore, the phase composition of the SiC powder was analysed using X-ray diffraction (XRD), as presented in Fig. 4(e). The results revealed the presence of two primary SiC phases: hexagonal SiC (6 H) and cubic SiC (3 C).

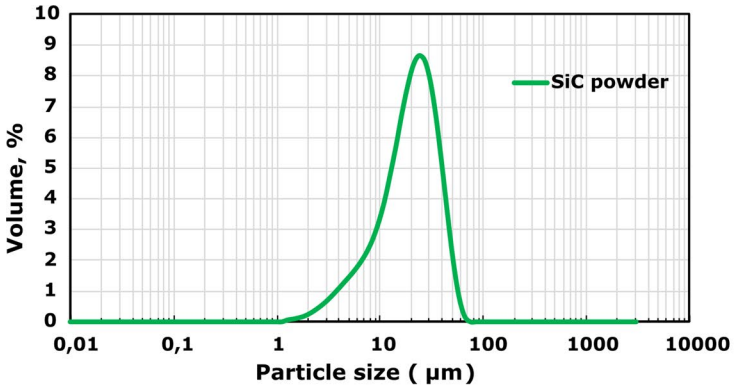
The samples were built using a ProX® DMP200 printer from the 3D Systems company. The printer features a fibre laser with a maximum power of 300 W, operating at a wavelength of 1060 nm, and provides a variable spot size. Square samples (10×10 mm^2) with a thickness of 0.2 mm were printed to examine SiC decomposition employing different strategies for laser scanning. The layer thickness and laser spot diameter were maintained consistently at 22 µm and 70 µm, respectively. The numerical model outlined in Sect. 2.1 was used to determine the optimal laser power and scanning speed necessary for evaluating different scanning strategies.

The Phoenix 3D printer can support multiple scanning strategies, as illustrated in Fig. 5. In the zigzag strategy, the hatching pattern is angled at a 45° angle. The hexagonal strategy utilised a hexagon size of 700 µm, with the inside laser-scanning pattern also inclined at 45° and randomly repeated across the layer. For all investigated scanning strategies, no inter-layer rotation was applied; the same scanning strategy was maintained across all layers. Argon was used to prevent and control oxidation during the D-LPBF. The process chamber was purged with argon at a continuous flow rate of 20 L/min, maintaining an oxygen level below 0.1% to ensure an inert atmosphere and prevent the formation of SiO_2. Finally, All samples were intentionally positioned at the center of the build platform to minimize variations associated with gas flow dynamics and powder spreading uniformity. Moreover, the ProX® DMP200 printer incorporates a patented recoating system consisting of a primary recoater blade followed by a secondary cylindrical element. This recoating mechanism ensures consistent powder delivery and improved uniformity across each deposited layer, thereby further mitigating any positional effects on powder bed quality.

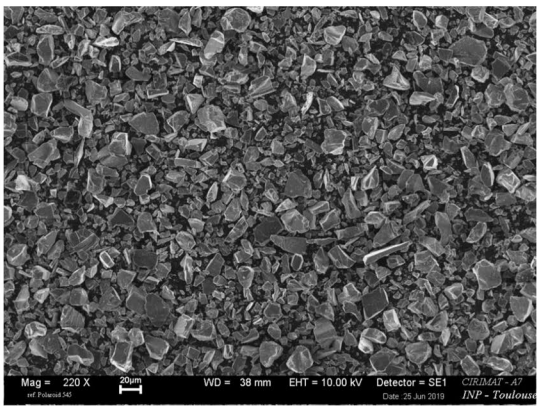
Fig. 4 Comprehensive characterisation of the SiC powder: (**a**) particle size distribution (PSD); (**b**) SEM micrograph of the SiC powder morphology; (**c**) SiC circular plates bonded to the printer baseplate; (**d**) smooth deposition of SiC powder on the SiC circular baseplate; and (e) XRD pattern of the SiC powder

2.2.2 Sample characterisation

Various characterisation approaches were employed to consider the quality of the printed SiC samples, including optical microscopic imaging and scanning electron microscopy (SEM) imaging. SEM images were also processed using ImageJ for quantitative porosity estimation as described in Sect. 3.4. For quantitative phase analysis, Rietveld XRD phase analysis was utilised. In the Rietveld Refinement, characteristics of the X-ray diffraction pattern, such as peak height, width, and position, are used to define aspects of the material's structure. The Rietveld refinement technique compares a theoretical pattern profile with a measured profile and refines it using the least-squares method. This study utilised Material Analysis Using Diffraction (MAUD) software for the Rietveld refinement of SiC powder and printed samples. Before refinement, the software was calibrated with LaB6 powder XRD diffraction to create a virtual XRD instrument within MAUD. This calibration process was required as various XRD instrument-related parameters within MAUD. The MAUD was used to analyse the SiC phases quantitatively after calibration.


Volume, %
Particle size (µm)
SiC powder
0,01
0,1
1
10
100
1000
10000

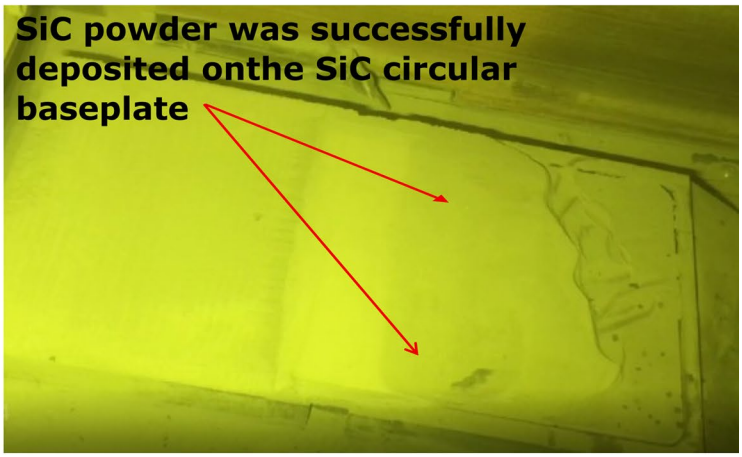
(a)


Mag = 220 X
20µm
WD = 38 mm
EHT = 10.00 kV
Detector = SE1
CIRIMAT - A7
INP - Toulouse

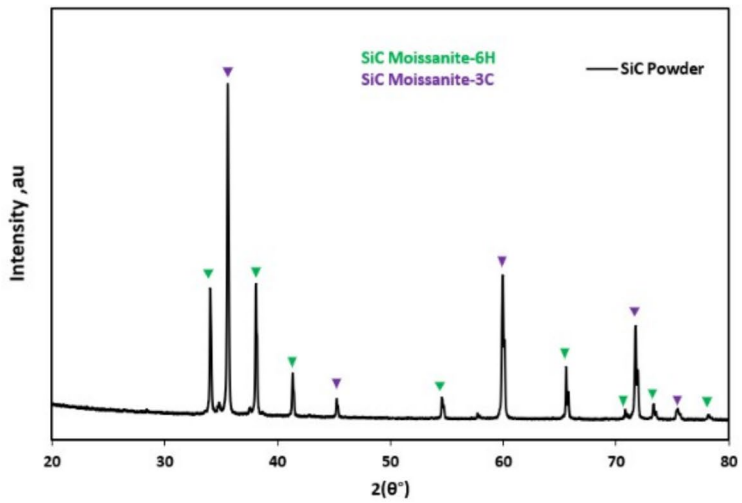
(b)



(c)


SiC powder was successfully deposited onthe SiC circular baseplate

(d)


SiC Moissanite-6H
SiC Moissanite-3C
SiC Powder
Intensity ,au
20
30
40
50
60
70
80
2(θ°)

(e)

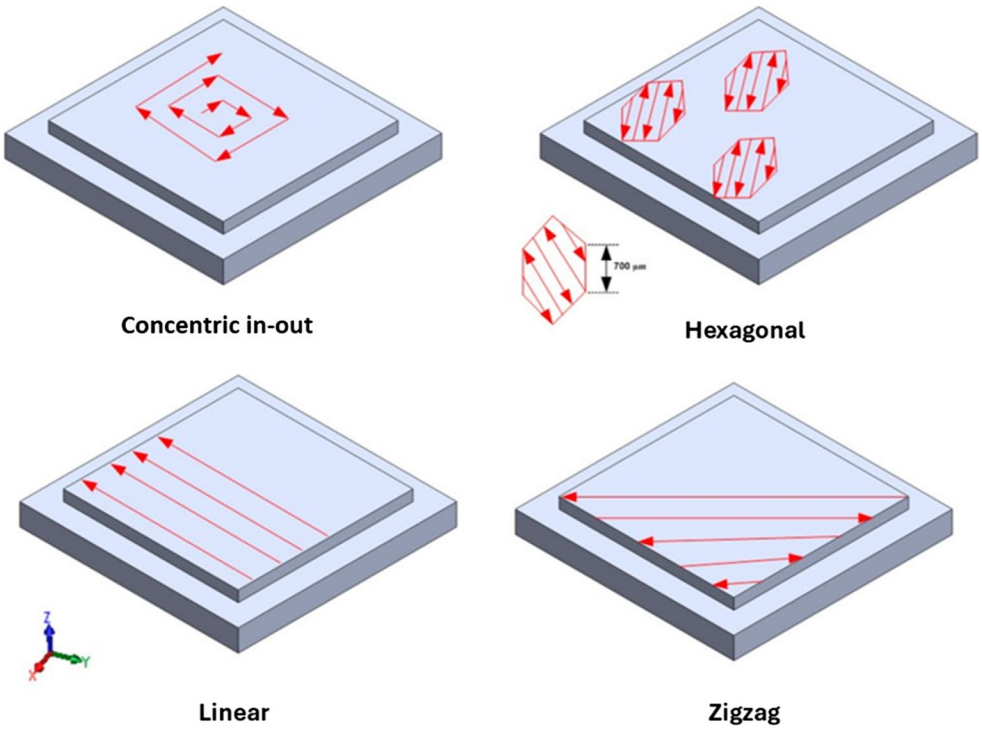


Fig. 5 Schematic illustration of the scanning strategies examined in this study [30], representing linear, concentric in-out, zigzag, and hexagonal patterns

3 Results and discussion

3.1 D-LPBF processing parameters

The selection of appropriate laser power and scanning speed is crucial for effectively applying the D-LPBF technique in ceramic material printing. A numerical model was used to determine the optimal laser parameters. Previous studies on LPBF have shown that slower scanning speeds are generally more efficient. Increased speeds can lead to powder dispersion due to the laser beam's inertia, which may negatively affect the quality of the printed components [35, 36]. This research employed a constant scanning speed of 250 mm/s and a hatching space of 35 µm to investigate the effect of various scanning strategies on the phase composition resulting from D-LPBF processing, based on the previous corpus [37]. The model was then run to determine the necessary power value of the laser to sinter the layer thickness. Figure 6 presents the results for various laser power settings, illustrating both the sintering depth in vertical cross-sections and the temperature distribution on the layer's top surface. The findings showed that a 40 W laser power was insufficient to fully sinter the 22 µm layer, whereas 45 W achieved complete sintering. At this power level, the peak surface temperature reached 3200 K, exceeding the point at which SiC decomposes (around 2.800 °C) [38]. Notably, this high temperature was confined to the laser's focal point. Table 3 summarises the processing parameters used in this study.

3.2 SiC samples and temperature profile

Investigating the thermal profile or history for various scanning strategies during the LPBF of SiC is crucial for understanding the decomposition behaviour of SiC and its correlation with the temperature history. This insight is essential for developing mitigation strategies and techniques to eliminate or reduce this decomposition during the D-LPBF of SiC. Therefore, the developed numerical model has been utilised to simulate real-world scenarios of different scanning strategies during the D-LPBF of SiC and obtain the temperature profile for each scanning strategy. Additionally, SiC samples were printed to investigate the decomposition occurring with each scanning strategy. Although the printed specimens in this study were as thin as 0.2 mm, the results provide preliminary insights into the fundamental effect of scanning strategies on the decomposition of SiC. The decomposition tendency is expected to increase with part thickness because thermal accumulation progressively raises the baseline temperature. Future work will therefore extend both the model and experiments to multi-layer builds to quantify this scaling effect and establish process windows for thicker SiC components. The following sections provide an in-depth analysis of the thermal history associated with various scanning strategies and a comprehensive examination of the corresponding printed SiC samples.

It is worth highlighting that the numerical model in the subsequent sections, while simulating various scanning strategies, considers only a single-layer scanning

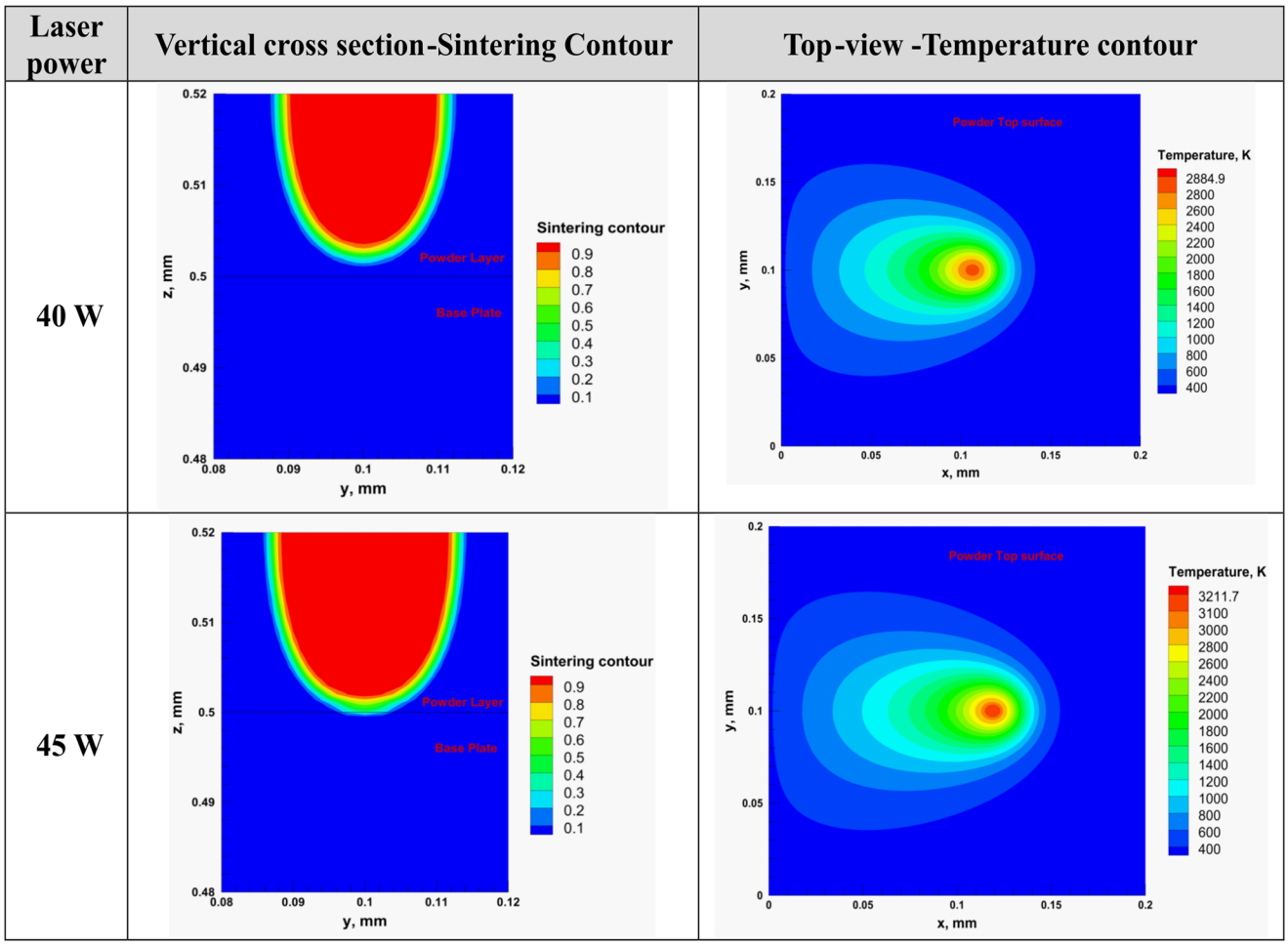


Fig. 6 Temperature distribution on the top surface of the layer and vertical cross-section sintering contours obtained with 40 W and 45 W laser power values and 250 mm/s scanning speed

Table 3 LPBF processing parameters used in this study

No	Item	Value
1	Laser power, W	45
2	Scanning speed, mm/s	250
3	Layer thickness, µm	22
4	Hatching space, µm	35
5	Inert gas	Argon

process, whereas the experimental setup involved ten layers. However, given the relatively small number of layers considered (10 layers) and the limited scanned area (approximately 10 mm²), the thermal profile across successive layers is expected to be nearly identical. The cooling time between consecutive layer scans allows sufficient dissipation of accumulated heat, resulting in comparable thermal conditions for each layer. Therefore, simulating a single layer provides a representative description of the process while significantly reducing computational cost and time, which are considerable in LPBF thermal modelling in this study.

3.2.1 Concentric in-out strategy

Figure 7 (a) displays SiC samples scanned with the concentric in-out strategy. For phase analysis, only ten deposited layers were examined to assess the impact of this scanning method. The manufactured parts exhibit various surface imperfections, including channels and voids. Figure 7(b) provides a detailed view of the top surface, revealing the distinct tracks created by the laser during the scanning process. Additionally, two intersecting lines forming an 'X' appear to be visible on the surface, with a small void at the centre of the intersection. This phenomenon is further investigated through simulations using the developed model to gain a better understanding of the dynamics involved in the scanning process.

Figure 8 illustrates the progression of the highest temperatures recorded while scanning with the concentric in-out method over approximately 70 ms. When the laser starts scanning, temperature spikes are particularly high due to the shorter scanning paths, which result in the formation of a

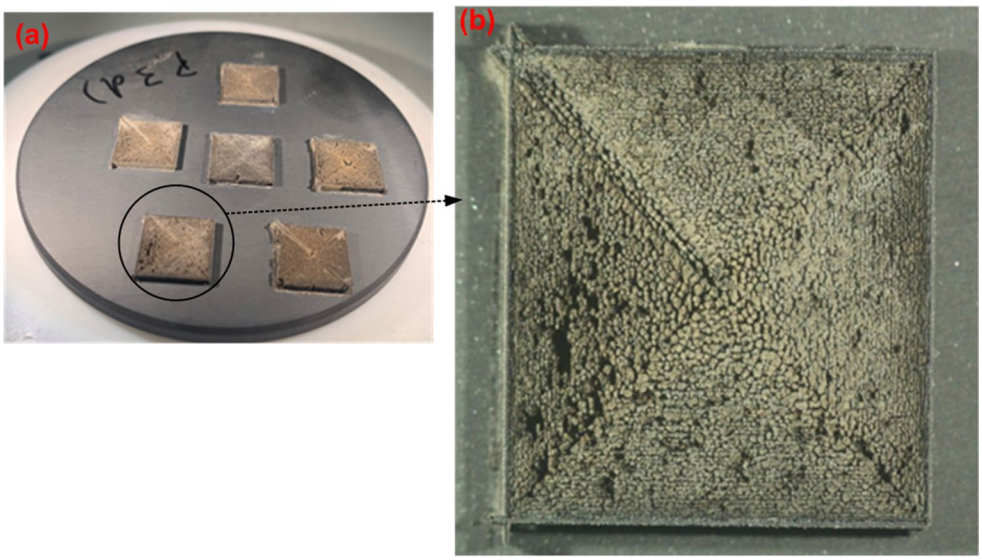


Fig. 7 SiC specimens (1 × 1 × 0.2 cm^3) scanned using the concentric in-out strategy: (**a**) as-built samples, (**b**) focused image of the layer top surface of the samples

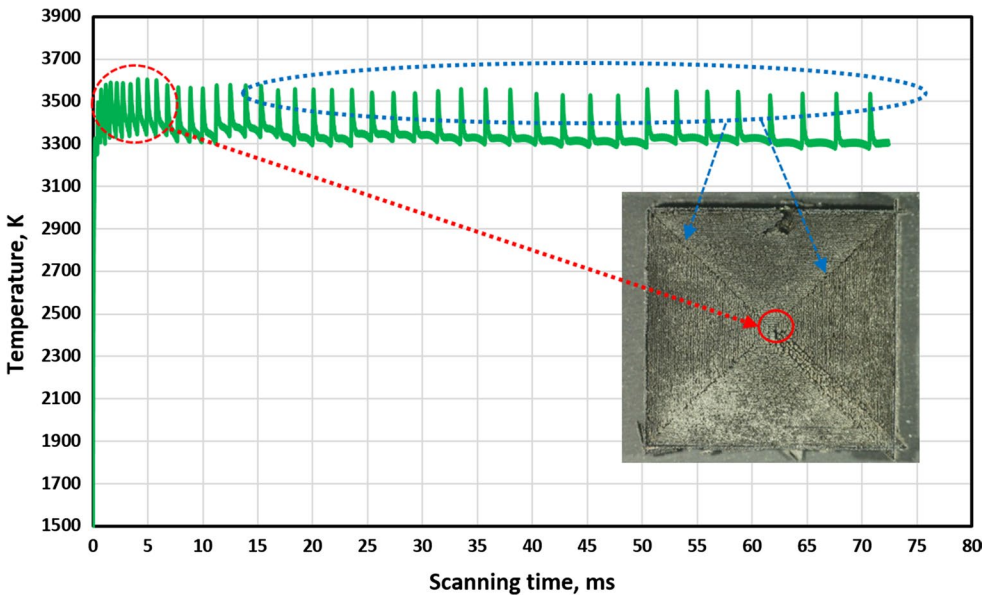


Fig. 8 Temperature progression history of the top surface scanned with the concentric in-out strategy

central hole in the specimen (highlighted by the dashed red circle). These temperature spikes recur periodically during scanning as the laser beam rotates at directional changes, creating an "X" mark on the sample's surface. Such temperature variations negatively affect SiC decomposition, as discussed in Section ß3.3. To improve this scanning strategy, it is essential to mitigate the heat buildup from short scanning paths and the temperature surges caused by the laser's rotation, both of which contribute to the decomposition of SiC.

SEM analysis was conducted on samples scanned using the concentric in-out strategy to assess the porosity and structure of the sintered SiC components (see Fig. 9). The layer surface displays a distinct arrangement of small protuberances aligned along the scanned rows parallel to the laser scanning directions. The scanning strategy and the variations in laser movement during the scanning process primarily influence this pattern. As the laser movement changes, the direction of these protuberances shifts accordingly. Additionally, there is a noticeable spacing between scanned rows of protuberances that follow the scanning paths, attributed to the hatching space used between scanning paths. The presence of these protrusions contributes to the elevated porosity observed in the SiC samples, which could potentially be mitigated by optimising powder bed properties in future research. Figure 9 also features a focused image highlighting the small protuberances, with the dark grey sintered SiC visible.

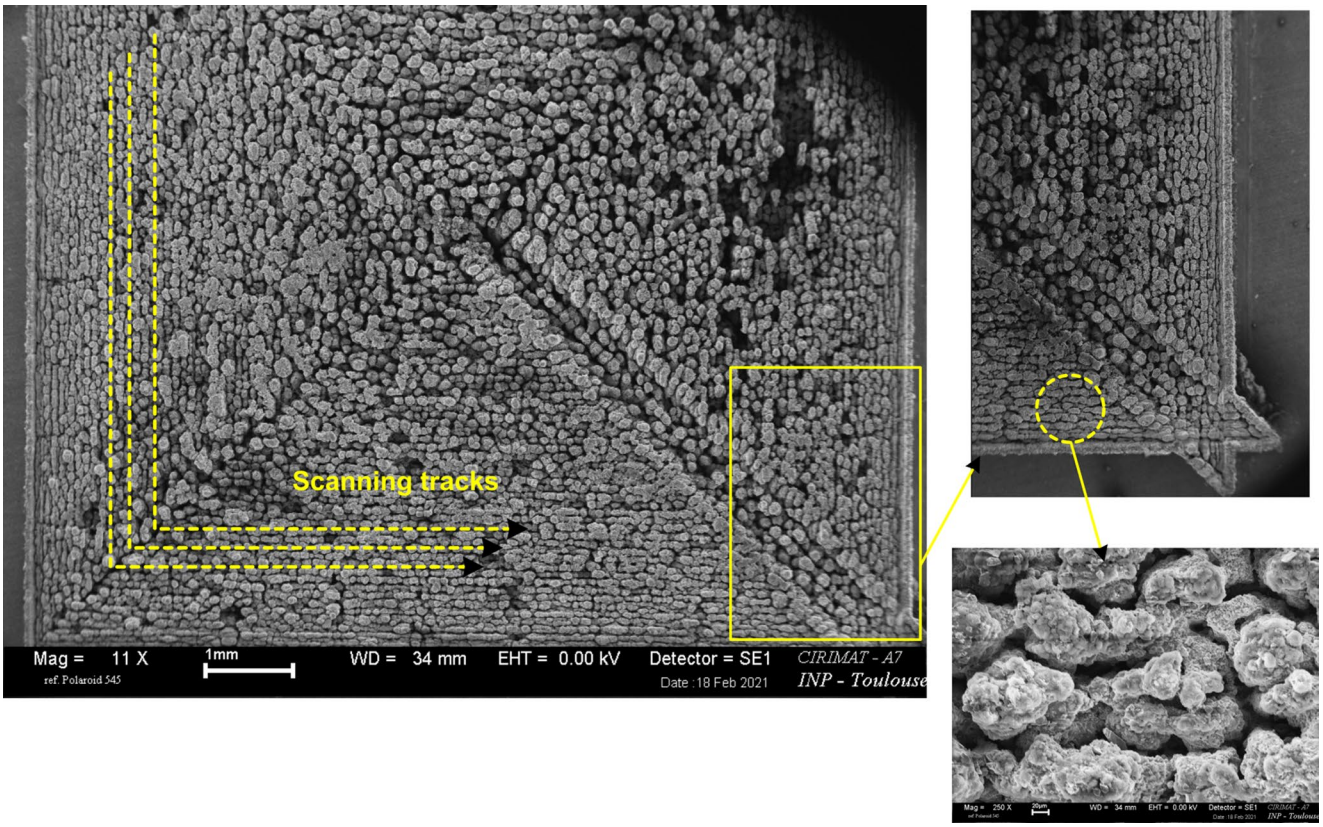


Fig. 9 SEM of the upper layer surface illustrating laser paths and defects resulting from the concentric in-out strategy

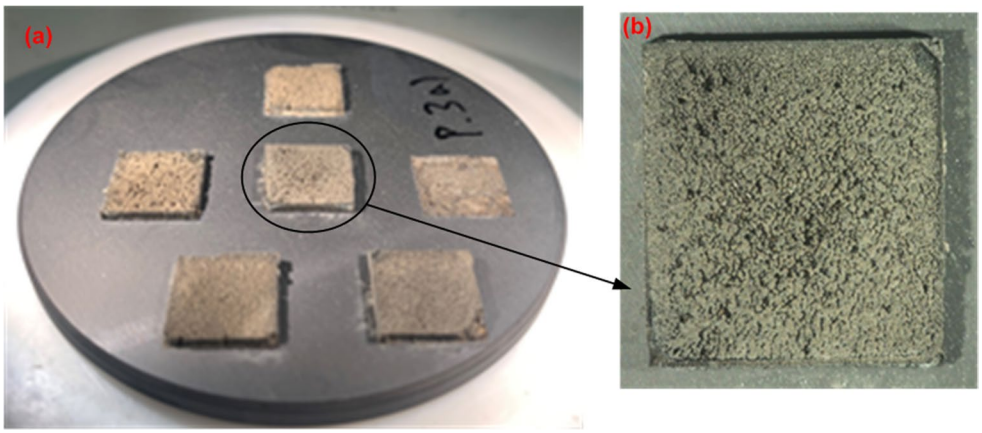


Fig. 10 SiC samples ($1 \times 1 \times 0.2$ cm³) built using the inclined zigzag strategy (a) and a focused view of the layer's upper surface

3.2.2 Inclined-Zigzag strategy

Figure 10(a) shows SiC samples fabricated using the inclined zigzag scanning approach, with a SiC disk serving as the baseplate. The samples display well-defined geometric forms, smooth surfaces, and straight edges, suggesting that this method holds promise for D-LPBF of SiC parts. In contrast to the samples produced with the concentric in-out technique, these samples feature flat surfaces without the characteristic patterns found in the latter. Visual inspection indicates that surface porosity is lower than that of the concentric in-out method. Despite the initial benefits of the zigzag approach, defects are present at the corners of the samples, as shown in Fig. 10(b). This close-up of a SiC sample printed using the inclined-linear strategy reveals small areas of material removal at the corners and visible small holes, indicating porosities.

The proposed model was employed to analyse the inclined zigzag scanning strategy and identify the root causes of the defects observed. Figure 11 illustrates the temperature profile for this scanning approach, where a limited number of paths were considered to reduce computational

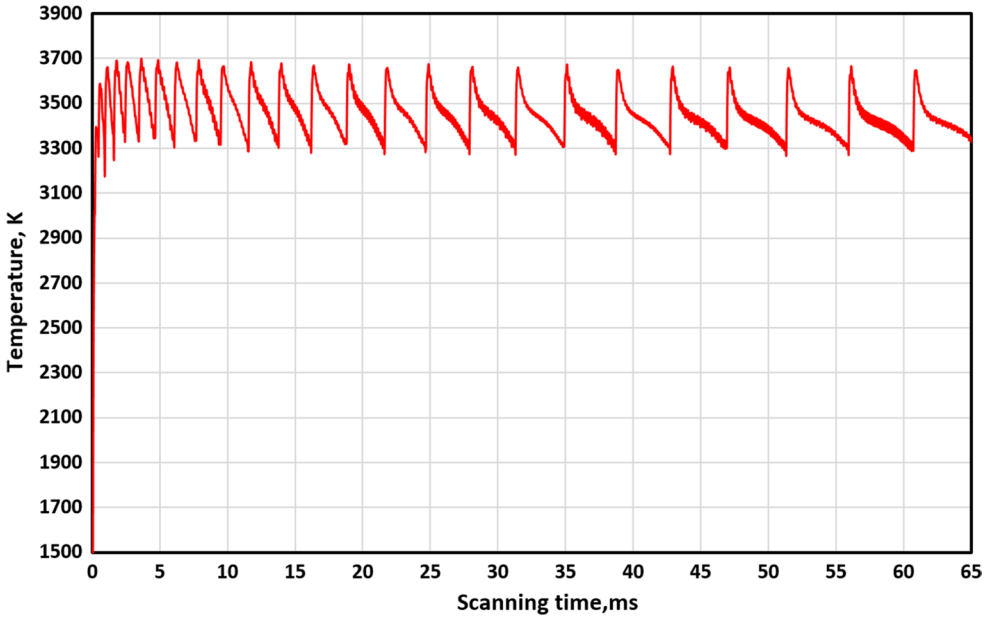


Fig. 11 Temperature progression history of the top surface scanned with the zigzag strategy (25 scanning tracks shown for clarity)

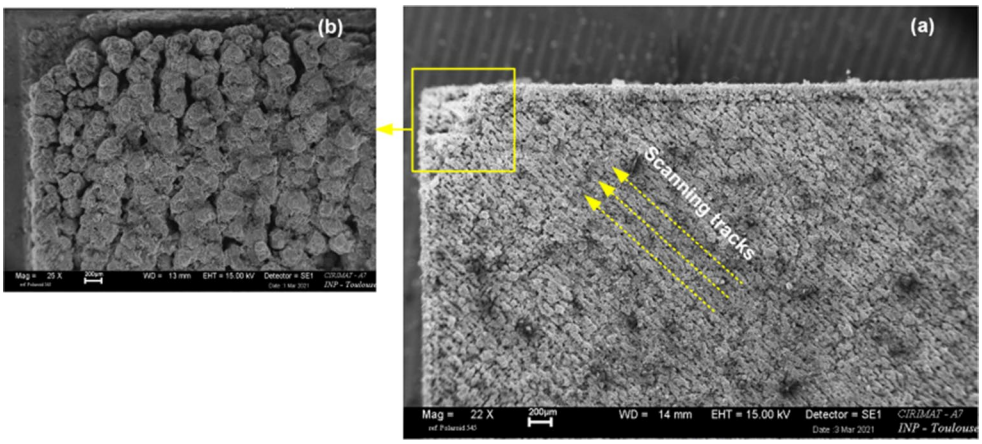


Fig. 12 SEM images of the top surface layer printed using the inclined zigzag strategy

load. It is evident that a significant temperature rise occurs as the laser completes one path and transitions to the next. In this approach, the laser's new starting point is positioned near the endpoint of the previous path, which retains residual heat and results in a sharp temperature increase. The temperature subsequently decreases gradually as the laser continues along the new path. Furthermore, the scanning time for each path progressively increases because the inclination in the scanning strategy extends the length of the scanning paths.

The temperature history obtained from numerical results using a zigzag scanning strategy shows periodic temperature fluctuations with peak values ranging from 3500 to 3600 K (Fig. 11). Although this temperature value approaches the SiC decomposition limit (~2800 °C), its short duration prevents significant decomposition. As the scan progresses, the interval between successive peaks gradually increases, indicating a gradual increase in cumulative heat accumulation. The decreasing temperature gradient slows the cooling rate, allowing the system to approach a quasi-steady thermal regime where energy input and dissipation are nearly balanced. This controlled thermal accumulation results in short, non-destructive overheating cycles that suppress SiC decomposition while promoting sintering.

SEM images showcasing the surface morphology of the top layer are shown in Fig. 12. Figure 12(a) shows that the inclined rows of raised features, aligned with the laser scanning paths, reflect the scanning strategy used on the top layer surface. These features form a uniform and smooth pattern, starkly contrasting with the unique X-pattern generated by the concentric in-out scanning strategy. The gaps between tracks are visible due to the hatching distance, so optimising parameters such as scanning speed and laser power is recommended. The raised features are also associated with porosity, similar to the concentric in-out strategy. Figure 12(b) provides a closer view of a specimen's corner, where localised heating in the narrow corner led to the decomposition and removal of SiC powder.

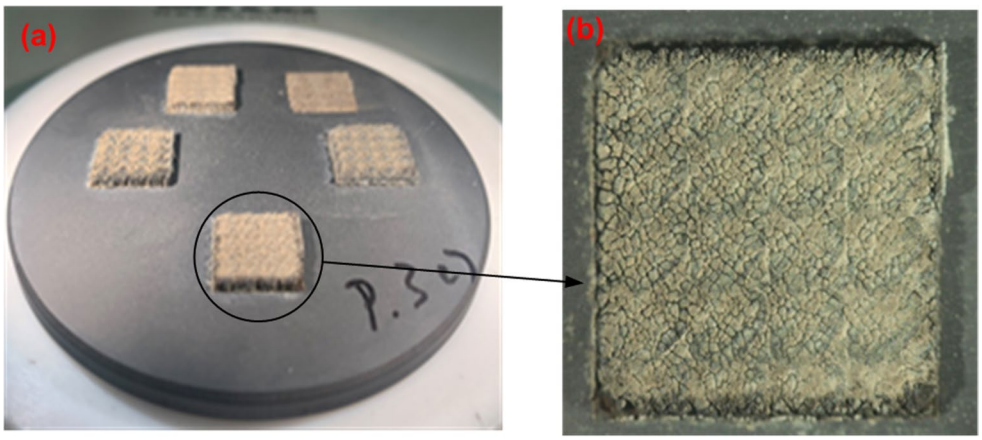


Fig. 13 SiC samples ($1 \times 1 \times 0.2$ cm^3) built using the hexagonal strategy (a) and focused view of the layer's upper surface

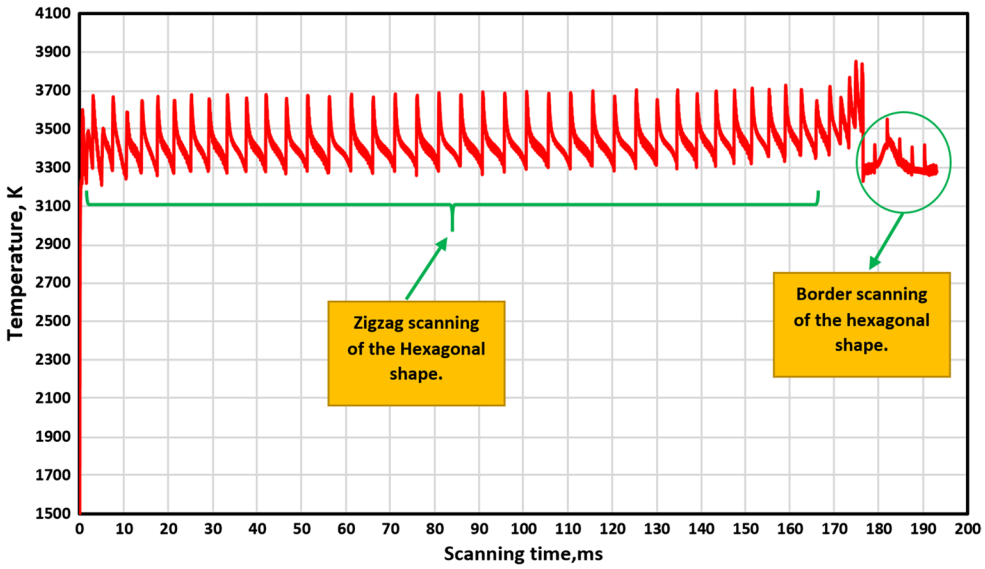


Fig. 14 Temperature progression history of the top surface scanned with the hexagonal strategy

3.2.3 Hexagonal strategy

Figure 13(a) illustrates printed SiC samples produced using the hexagonal scanning method, which delivered the best performance for LPBF processing of SiC. The samples exhibit distinct square geometries with minimal surface irregularities, except for faint hexagonal patterns visible on the uppermost layer. In addition, minor porosity is evident, appearing as isolated, tiny voids scattered across the surface.

The numerical simulation was employed to investigate the hexagonal scanning strategy, with the corresponding temperature distribution depicted in Fig. 14. The zigzag pattern within the hexagonal layout is visible, revealing a significant temperature spike when the laser initiates each new path. This temperature increase represents a key challenge for this scanning technique. After completing the zigzag phase, the process transitions to border scanning, demonstrating a comparatively lower temperature profile. This variation is attributed to the continuous and longer paths of border scanning, as opposed to the shorter, more interrupted zigzag paths. The temperature elevation caused by the zigzag pattern primarily impacts the central region of the part, whereas it has a minimal effect on the edges, unlike the inclined zigzag strategy.

Figure 15(a) displays the microstructure of the topmost surface layer, characterised by an almost solid appearance with very low porosity. The sintered particles are densely packed and are separated by a web of microchannels, as illustrated in Fig. 15(b). These microchannels indicate the high relative density achievable with this scanning method. A detailed view of the SiC particles and the microchannels is provided in Fig. 15(c).

3.2.4 Linear strategy

Figure 16(a) displays SiC samples printed using the linear strategy, with a focus on a thickness of 0.2 mm to study the effects of this strategy. The samples show numerous defects, including damaged edges and porosities. Additionally, layer shifting is observed, as illustrated in the microscopic view in

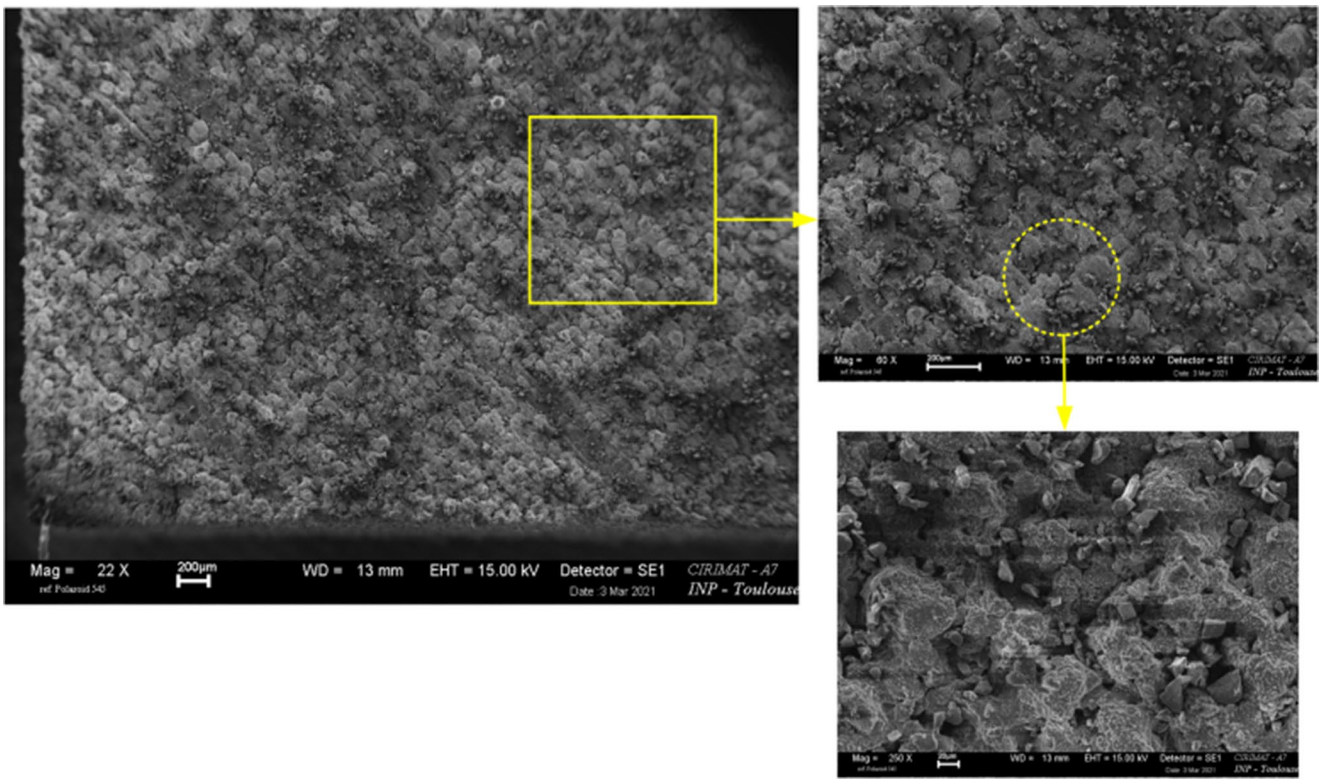


Fig. 15 SEM images of SiC specimens scanned using the hexagonal strategy

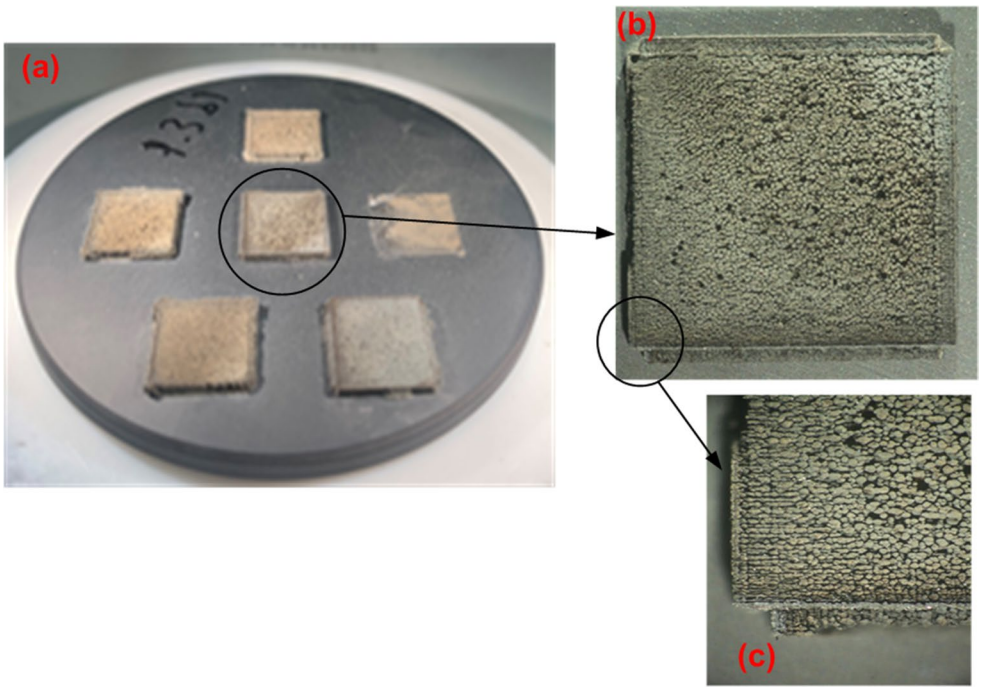


Fig. 16 SiC samples ($1 \times 1 \times 0.2$ cm^3) printed using the linear scanning strategy: (**a**) overall view of the as-built samples on the substrate, (**b**) magnified view of the upper surface, and (c) detailed surface region showing incomplete sintering, pore distribution, and sharp corner formation

Fig. 16(b). This shifting is problematic because it affects the dimensional accuracy of the printed part. A numerical model was employed to understand the cause of this shift. The maximum temperature history from the numerical model, shown in Fig. 17, reveals several temperature dips at the beginning of each scanning path. These dips are attributed to the time when the laser is turned off while repositioning for the next scan, followed by the time needed to heat the SiC powder to its sintering temperature. Layer shifting can occur when consecutive layers do not adequately adhere,

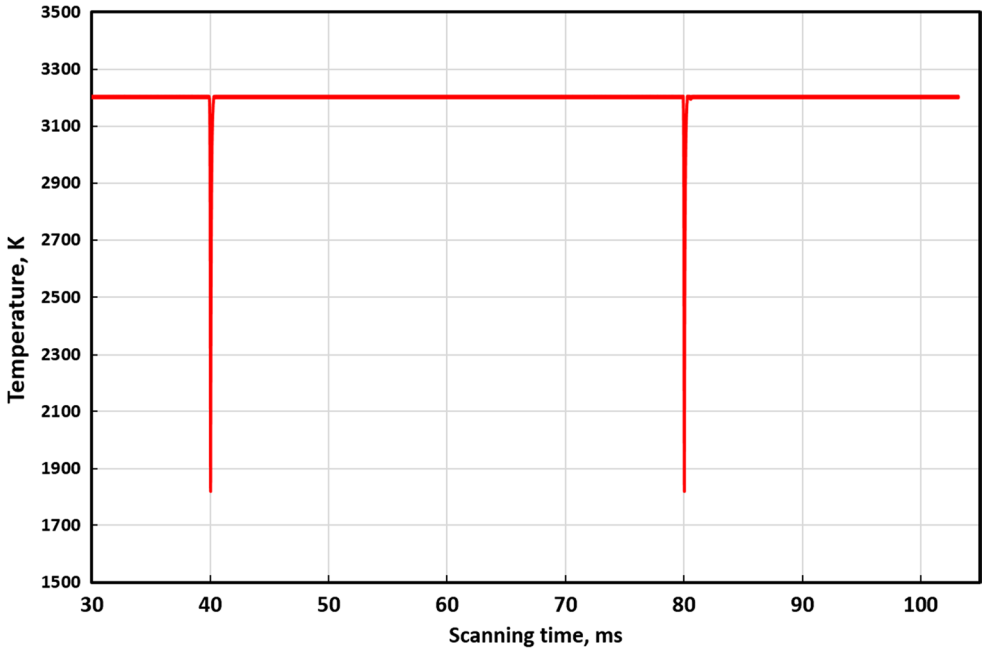


Fig. 17 Temperature progression history of the top surface scanned with the linear strategy

with the recoater's force sufficient to cause this movement. This issue is evident from the temperature history of this scanning strategy, where the scanning temperature reaches around 3200 K. Although this temperature is sufficient for sintering the 22 µm layer, it is inadequate for achieving proper adhesion to the underlying layer.

In contrast, other scanning strategies with temperature peaks during scanning facilitated better layer adhesion, providing enough support to resist the recoater's force. However, the linear strategy's lack of temperature peaks during scanning led to poor adhesion and subsequent layer shifting. Raising the laser power to resolve this issue is not recommended, as it would surpass the decomposition threshold of SiC.

Figure 18 displays the sintering contours for the linear strategies, inclined zigzag, and concentric in-out methods, illustrating both the top surface and a cross-sectional plane to assess the sintering depth. For the linear strategy, the vertical section (yz section at x = 0.1 mm) plane shows either no bonding or minimal bonding between the current scanned layer and the one beneath it. This lack of strong adhesion leads to the layer shifting observed with this strategy. Conversely, the other scanning methods show distinct adhesion between layers, effectively preventing such shifting. The hexagonal method demonstrates the deepest adhesion, indicating the most effective layer bonding among all the strategies.

Figure 19 shows the SEM images of the sintered structure of SiC samples fabricated using the linear scanning strategy. Consistent with previous methods, the top surface exhibits a clear pattern of small, raised features arranged in linear rows, aligned with the scanning paths, with the spacing determined by the hatching distance. The images also reveal a notable amount of porosity. Quantitative areal porosity was determined from representative SEM images using ImageJ by threshold segmentation and particle analysis. The resulting values (25.73%, 9.99%, 6.30%, and 21.59% for Figs. 9, 12 and 15, and 19, respectively) confirmed that the hexagonal and zigzag strategies yielded the lowest areal porosity. These findings suggest that the linear scanning strategy is unsuitable for SiC LPBF processing.

3.3 Rietveld XRD phase analysis

Quantitative analysis of SiC phases poses challenges with traditional X-ray diffraction due to the overlapping diffraction peaks of different SiC phases. To accurately analyse SiC phases across the studied scanning strategies and assess the impact of temperature history on each sample, we employed the Rietveld method, as detailed by Hongchao and Changlin [39]. Figure 20 displays the X-ray diffraction spectra for the feedstock powder and SiC samples scanned using concentric in-out, inclined zigzag, and hexagonal strategies (the linear strategy was excluded due to layer shifting, rendering it unsuitable for D-LPBF of SiC). The feedstock powder shows the presence of two SiC phases: SiC-6 H and SiC-15R. Post-LPBF, additional carbon and silicon phases emerged, indicating SiC decomposition. Despite the parameters being adequate to sinter SiC particles without decomposition, temperature peaks during scanning with different strategies contributed to this phase transformation. Table 4 lists the quantities of each phase in the SiC powder and the SiC samples processed with various scanning strategies. The hexagonal strategy displayed more silicon and

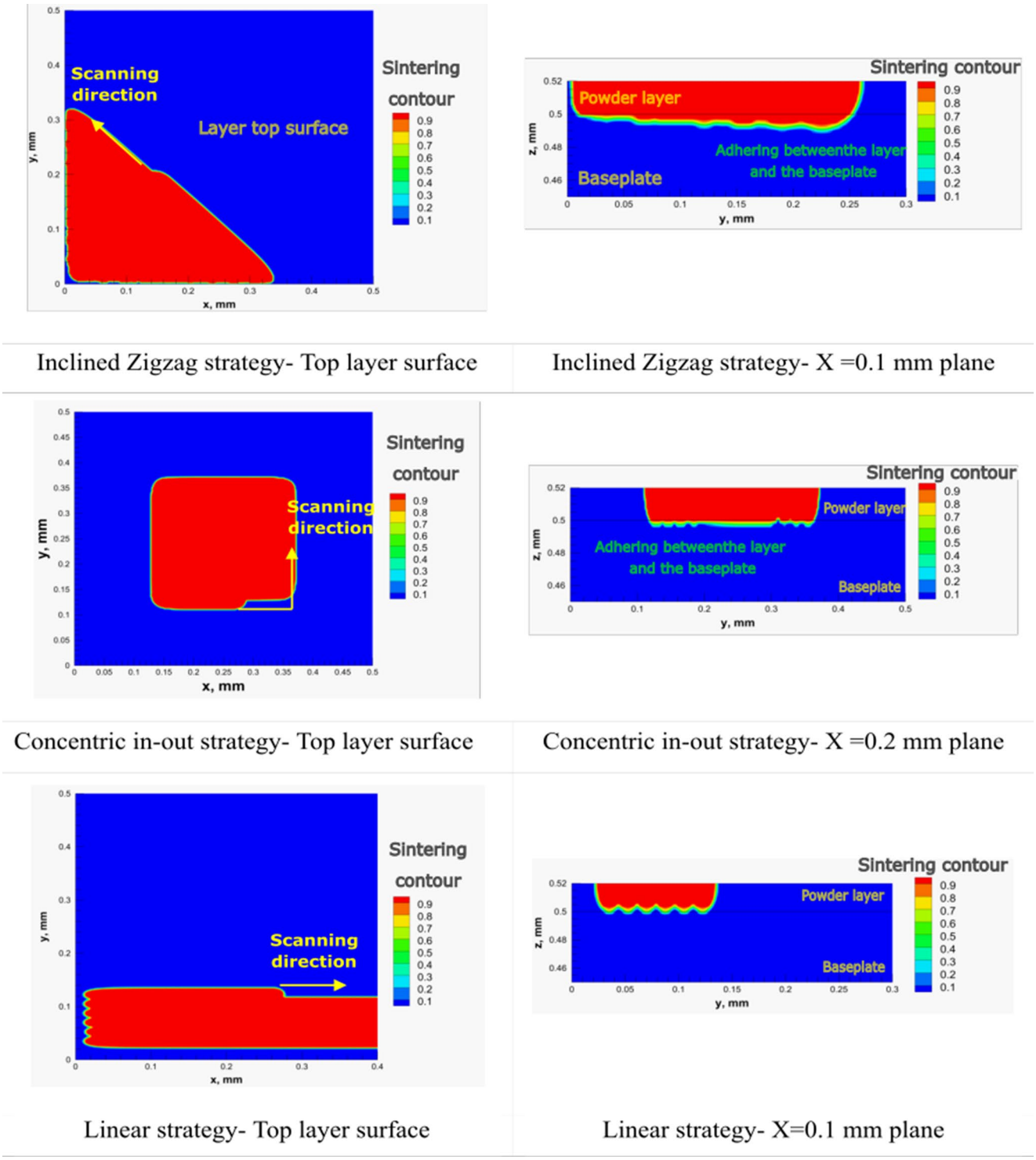


Fig. 18 Sintering phase progression with the employed scanning strategy at different locations as indicated

carbon than the concentric in-out and zigzag strategies, indicating greater SiC decomposition. This increased decomposition in the hexagonal strategy is attributed to the very short and numerous laser track paths, which created temperature peaks at the start of each new path. In the concentric in-out strategy, decomposition mainly occurred at points where the laser changed direction, generating temperature peaks as previously described. Conversely, the zigzag strategy exhibited lower decomposition than the concentric in-out and hexagonal strategies because temperature peaks were

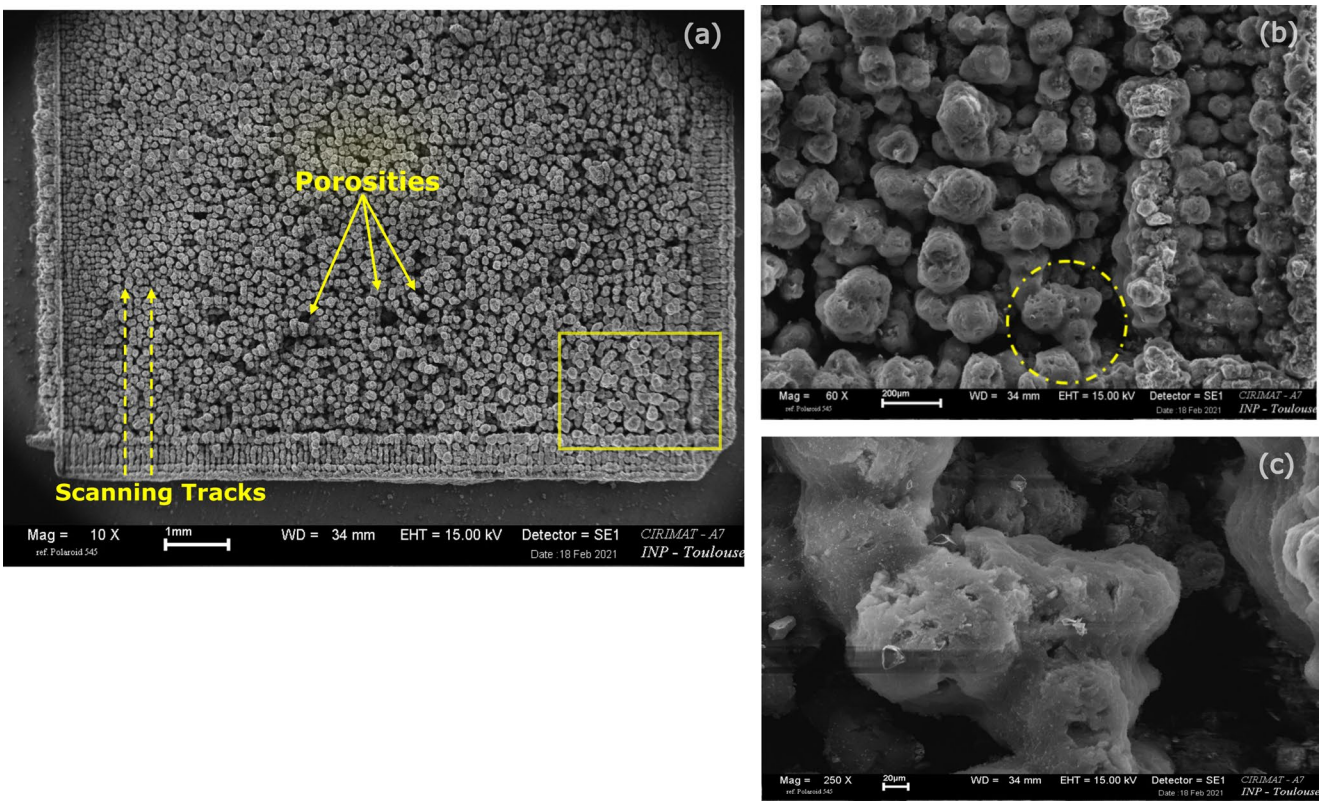


Fig. 19 SEM images of SiC samples printed using the linear scanning strategy

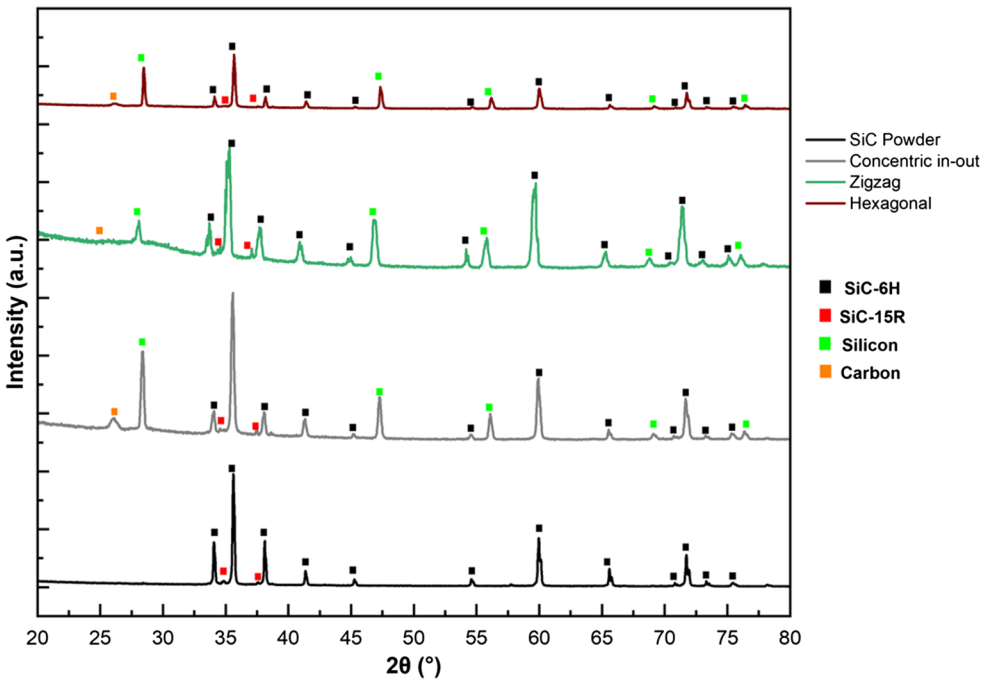


Fig. 20 X-ray diffraction (XRD) spectra of SiC printed using various scanning strategies

confined to the borders rather than within the scanning area. Developing a new scanning strategy is crucial for mitigating these temperature peaks and preventing SiC decomposition. However, current limitations with the 3D printer software hinder such modifications. Future advancements in SiC LPBF printers should focus on developing new scanning strategies designed explicitly for ceramics to address these issues effectively. The significant decomposition observed

Table 4 SiC phase quantity at different scanning strategies

Strategy	SiC Powder	Concentric In-out	Zigzag	Hexagonal
SiC-6 H	97.63% ± 9.03	78.99% ± 1.85	87.48% ± 2.3	76.31% ± 0.05
SiC-15R	2.36% ± 0	2.01% ± 00	4.61E-4% ± 00	0
Silicon	-	15.77% ± 0.35	8.84% ± 0.694	18.01% ± 0.01
Carbon	-	3.25% ± 0.15	1.07% ± 0.694	5.66% ± 0.014
R_{wp} (%)	8.53	14.07	17.56	14.04
R_{exp} (%)	4.20	4.93	4.601	4.79

in the hexagonal scanning strategy is due to heat accumulation behaviour. In this scanning strategy, the laser beam is traced through short, adjacent scan tracks before completing a discrete boundary traversal. Each new scan results in a rapid increase in temperature due to localised heat accumulation at the scan starting point. Frequent microheating causes multiple transient temperature peaks that exceed the SiC decomposition threshold (~ 2800 °C) and cause the SiC to decompose into Si and C.

Furthermore, adjacent short laser lines, due to the limited time available for heat transfer, create overlapping high-temperature thermal zones. This accumulation further increases the peak temperature. Repeated peak formations, in turn, reduce the thermochemical stability of SiC. In contrast, zigzag and concentric in-out strategies create a more uniform heat distribution across the scanned area, reducing the frequency and intensity of temperature overshoots responsible for decomposition. The emergence of separate Si and C phases due to SiC decomposition is expected to impact the mechanical integrity of printed parts negatively. The silicon phase is softer than SiC, and the tendency for carbon to accumulate in pores and along grain boundaries acts as crack initiation sites in the printed sample. For instance, it has been reported in the literature that microstructural heterogeneity, including phase distribution and grain boundary characteristics in SiC structures, affects the fracture toughness of silicon carbide materials [40]. Because the resulting heterogeneous structure is expected to reduce strength, future studies investigating mechanical behaviour should be planned.

4 Conclusions and future study

Direct Laser Powder Bed Fusion (D-LPBF) of SiC poses a considerable challenge due to the risk of SiC decomposition at high temperatures during the sintering process. This study developed a numerical model to predict optimal laser sintering parameters, such as laser power and scanning speed, and evaluated their effectiveness across various scanning strategies, including linear, hexagonal, zigzag, and concentric in-out. The results indicated that the linear strategy is unsuitable for SiC D-LPBF due to issues with layer shifting. To mitigate layer shifting observed in the linear strategy in D-LPBF of SiC, this can contribute to future studies that apply short-strip or alternating scanning strategies or preheating techniques to improve interlayer adhesion without exceeding the SiC segregation threshold. The concentric in-out strategy also proved ineffective due to creating distinctive surface patterns. Conversely, both the zigzag and hexagonal strategies successfully avoided these problems. X-ray diffraction and quantitative phase analysis of SiC samples produced using various scanning strategies revealed decomposition into silicon and carbon. This decomposition was attributed to temperature peaks generated by the scanning strategies, which exceeded the decomposition point of SiC, leading to the formation of silicon and carbon within the SiC parts. significant variations in phase retention and by-product formation. For the SiC-6 H powder, the Concentric In–Out strategy resulted in the highest retention (97.63% ± 9.03), followed by the Zigzag (87.48% ± 2.3) and Hexagonal (76.31% ± 0.05) strategies. In contrast, the SiC-15R phase was almost completely decomposed under all scanning strategies, with negligible residual content. Silicon and carbon by-products were observed to accumulate differently depending on the scanning strategy; for instance, the Hexagonal strategy resulted in the highest silicon (18.01% ± 0.01) and carbon (5.66% ± 0.014) content. These results demonstrate that scanning strategy strongly influences the thermal decomposition behavior and phase evolution of SiC during D-LPBF, providing a quantitative foundation for optimizing processing conditions in future studies.Developing new scanning strategies is crucial for advancing the successful D-LPBF of SiC.

Authors contribution Mohamed Abdelmoula and Alejandro Montón Zarazaga carried out the research for this study and were responsible for writing and organising the final manuscript. All authors reviewed and approved the final version of the manuscript.

Funding Open access funding provided by the Scientific and Technological Research Council of Türkiye (TÜBİTAK). This project has been funded by the European Union's Horizon 2020 Framework Program for Research and Innovation (2014–2020) under the Marie Skłodowska-Curie Grant Agreement No. [764935].

Data availability The authors confirm that the data supporting the results of this study are available in the article and/or its supplementary materials.

Declarations

Ethical approval All relevant international, national, and/or institutional guidelines for the care and use of research materials were adhered to.

Consent to participate Not applicable.

Consent for publication The authors grant the publisher permission to publish the work.

Competing interests The authors declare no conflicts of interest or competing interests.

Open Access This article is licensed under a Creative Commons Attribution 4.0 International License, which permits use, sharing, adaptation, distribution and reproduction in any medium or format, as long as you give appropriate credit to the original author(s) and the source, provide a link to the Creative Commons licence, and indicate if changes were made. The images or other third party material in this article are included in the article's Creative Commons licence, unless indicated otherwise in a credit line to the material. If material is not included in the article's Creative Commons licence and your intended use is not permitted by statutory regulation or exceeds the permitted use, you will need to obtain permission directly from the copyright holder. To view a copy of this licence, visit http://creativecommons.org/licenses/by/4.0/.

References

1. Xun Q, Xun B, Li Z et al (2017) Application of SiC power electronic devices in secondary power source for aircraft. Renew Sustain Energy Rev 70:1336–1342. https://doi.org/10.1016/j.rser.2016.12.035
2. Murayama N, Hirao K, Sando M et al (2018) High-temperature electro-ceramics and their application to SiC power modules. Ceram Int 44:3523–3530. https://doi.org/10.1016/j.ceramint.2017.11.140
3. KIM W-J, KIM D, PARK JY, FABRICATION AND MATERIAL ISSUES FOR THE APPLICATION OF SiC COMPOSITES TO LWR FUEL CLADDING (2013) Nuclear Eng Technol 45:565–572. https://doi.org/10.5516/NET.07.2012.084
4. Cui Y, Wang L, Ren J (2008) Multi-functional SiC/Al composites for aerospace applications. Chin J Aeronaut 21:578–584. https://doi.org/10.1016/S1000-9361(08)60177-6
5. Hunter GW, Neudeck PG, Xu J et al (2004) Development of SiC-based Gas Sensors for Aerospace Applications. MRS Proceedings 815:J4.4. https://doi.org/10.1557/PROC-815-J4.4
6. Choyke WJ, Pensl G (1997) Physical properties of SiC. MRS Bull 22:25–29. https://doi.org/10.1557/S0883769400032723
7. Wu IJ, Guo GY (2007) Optical properties of SiC nanotubes. Phys Rev B 76:035343. https://doi.org/10.1103/PhysRevB.76.035343
8. Gubernat A, Stobierski L, Łabaj P (2007) Microstructure and mechanical properties of silicon carbide pressureless sintered with oxide additives. J Eur Ceram Soc 27:781–789. https://doi.org/10.1016/j.jeurceramsoc.2006.04.009
9. Fantozzi G, Niepce J-C, Bonnefont G et al (2013) Industrial ceramics-Properties, forming and applications; Les ceramiques industrielles-Proprietes, mise en forme et applications
10. Grossin D A review of additive manufacturing of ceramics by powder bed selective laser processing (sintering / melting): Calcium Phosphate, Silicon Carbide, Zirconia, Alumina, and their composites. 93
11. Gonzalez JA (2016) Characterization of ceramic components fabricated using binder jetting additive manufacturing technology. Ceram Int 6
12. Hu C, Chen Y, Liu H et al (2021) Effect of SiC powder on the properties of SiC slurry for stereolithography. Ceram Int. https://doi.org/10.1016/j.ceramint.2021.01.101
13. Jin L, Zhang K, Xu T et al (2018) The fabrication and mechanical properties of SiC/SiC composites prepared by SLS combined with PIP. Ceram Int 44:20992–20999. https://doi.org/10.1016/j.ceramint.2018.08.134
14. Montón A, Abdelmoula M, Küçüktürk G et al (2021) Experimental and numerical study for direct powder bed selective laser processing (sintering/melting) of silicon carbide ceramic. Mater Res Express 8:045603. https://doi.org/10.1088/2053-1591/abf6fc
15. Meyers S, De Leersnijder L, Vleugels J, Kruth J-P (2018) Direct laser sintering of reaction bonded silicon carbide with low residual silicon content. J Eur Ceram Soc 38:3709–3717. https://doi.org/10.1016/j.jeurceramsoc.2018.04.055
16. Liu K, Wu T, Bourell DL et al (2018) Laser additive manufacturing and homogeneous densification of complicated shape SiC ceramic parts. Ceram Int 44:21067–21075. https://doi.org/10.1016/j.ceramint.2018.08.143
17. Streek A, Regenfuß P, Ullmann F et al Processing of silicon carbide by laser micro sintering. 10
18. Löschau W, Lenk R, Scharek S et al (2000) Prototyping of Complex-Shaped parts and tools of Si/SiC-Ceramics. Ind Ceram 38:6. https://doi.org/10.1002/3527607293.ch24
19. Geng J, Yin J, Wang L et al (2025) Direct selective laser sintering and properties of SiC ceramics doped with Al2O3–Y2O3. J Am Ceram Soc 108:e70102. https://doi.org/10.1111/jace.70102
20. Wang Y, Wang P, Li L et al (2025) Effect of Si addition on microstructure and mechanical properties of SiC ceramic fabricated by direct LPBF with CVI technology. Appl Sci 15:8585. https://doi.org/10.3390/app15158585
21. Hwa LC, Rajoo S, Noor AM et al (2017) Recent advances in 3D printing of porous ceramics: a review. Curr Opin Solid State Mater Sci 21:323–347. https://doi.org/10.1016/j.cossms.2017.08.002
22. Mostafaei A, Elliott AM, Barnes JE et al (2021) Binder jet 3D printing—process parameters, materials, properties, modeling, and challenges. Prog Mater Sci 119:100707. https://doi.org/10.1016/j.pmatsci.2020.100707
23. ZTA Ceramic Materials for DLP 3D Printing - IOPscience https://iopscience.iop.org/article/10.1088/1757-899X/678/1/012020/meta. Accessed 5 Nov 2025
24. Zheng Y, Zhang K, Liu TT et al (2019) Cracks of alumina ceramics by selective laser melting. Ceram Int 45:175–184. https://doi.org/10.1016/j.ceramint.2018.09.149
25. Qiu Y-D, Wu J-M, Chen A-N et al (2020) Balling phenomenon and cracks in alumina ceramics prepared by direct selective laser melting assisted with pressure treatment. Ceram Int 46:13854–13861. https://doi.org/10.1016/j.ceramint.2020.02.178
26. Yves-Christian H, Jan W, Wilhelm M et al (2010) Net shaped high performance oxide ceramic parts by selective laser melting. Phys Procedia 5:587–594. https://doi.org/10.1016/j.phpro.2010.08.086
27. Liu Q, Danlos Y, Song B et al (2015) Effect of high-temperature preheating on the selective laser melting of yttria-stabilized zirconia ceramic. J Mater Process Technol 222:61–74. https://doi.org/10.1016/j.jmatprotec.2015.02.036
28. Montón Zarazaga A, Abdelmoula M, Küçüktürk G et al (2022) Process parameters investigation for direct powder bed selective laser processing of silicon carbide parts. Prog Addit Manuf. https://doi.org/10.1007/s40964-022-00305-7
29. Abdelmoula M, Küçüktürk G, Grossin D et al (2023) Direct selective laser sintering of silicon carbide: realizing the full potential

through process parameter optimization. Ceram Int. https://doi.org/10.1016/j.ceramint.2023.07.189
30. Abdelmoula M, Zarazaga AM, Küçüktürk G et al (2022) Scanning strategy investigation for direct powder bed selective laser processing of silicon carbide ceramic. Appl Sci 12:788. https://doi.org/10.3390/app12020788
31. Moser D, Fish S, Beaman J, Murthy J (2014) Multi-Layer computational modeling of selective laser sintering processes. Volume 2A: advanced manufacturing. American Society of Mechanical Engineers, Montreal, Quebec, Canada. V02AT02A008
32. Groth R, Kauer E (1961) Absorption Freier Ladungsträger in α-SiC-Kristallen. Phys Stat Sol (b) 1:445–450. https://doi.org/10.1002/pssb.19610010504
33. Yablokova G, Speirs M, Van Humbeeck J et al (2015) Rheological behavior of β-Ti and NiTi powders produced by atomization for SLM production of open porous orthopedic implants. Powder Technol 283:199–209. https://doi.org/10.1016/j.powtec.2015.05.015
34. Powder flowability characterisation methodology for powder-bed-based metal additive manufacturing | Progress in Additive Manufacturing. https://link.springer.com/article/10.1007/S40964-015-0001-4. Accessed 5 Nov 2025
35. Fan Z, Lu M, Huang H (2018) Selective laser melting of alumina: a single track study. Ceram Int 44:9484–9493. https://doi.org/10.1016/j.ceramint.2018.02.166
36. Ahn IH (2019) Determination of a process window with consideration of effective layer thickness in SLM process. Int J Adv Manuf Technol 105:4181–4191. https://doi.org/10.1007/s00170-019-04402-w
37. Abdelmoula M, Küçüktürk G, Grossin D et al (2023) Direct selective laser sintering of silicon carbide: realizing the full potential through process parameter optimization. Ceram Int 49:32426–32439. https://doi.org/10.1016/j.ceramint.2023.07.189
38. Kang H-K, Kang SB (2006) Thermal decomposition of silicon carbide in a plasma-sprayed Cu/SiC composite deposit. Mater Sci Engineering: A 428:336–345. https://doi.org/10.1016/j.msea.2006.05.054
39. Hongchao L, Changlin K Quantitative analysis of SiC polytype distributions by the Rietveld method. 4
40. Fan Z, Zhang J, Wang Z et al (2024) A state-of-the-Art review of fracture toughness of silicon carbide: implications for high-precision laser dicing techniques. Processes 12:2696. https://doi.org/10.3390/pr12122696

Publisher's note Springer Nature remains neutral with regard to jurisdictional claims in published maps and institutional affiliations.